

# Biomimetic optic flow sensing applied to a lunar landing scenario

Florent Valette, Franck Ruffier, Stéphane Viollet, and Tobias Seidl

**Abstract**— Autonomous landing on unknown extraterrestrial bodies requires fast, noise-resistant motion processing to elicit appropriate steering commands. Flying insects excellently master visual motion sensing techniques to cope with highly parallel data at a low energy cost, using dedicated motion processing circuits. Results obtained in neurophysiological, behavioural, and biorobotic studies on insect flight control were used to safely land a spacecraft on the Moon in a simulated environment. ESA’s Advanced Concepts Team has identified autonomous lunar landing as a relevant situation for testing the potential applications of innovative bio-inspired visual guidance systems to space missions. Biomimetic optic flow-based strategies for controlling automatic landing were tested in a very realistic simulated Moon environment. Visual information was provided using the PANGU software program and used to regulate the optic flow generated during the landing of a two degrees of freedom spacecraft. The results of the simulation showed that a single elementary motion detector coupled to a regulator robustly controlled the autonomous descent and the approach of the simulated moonlander. “Low gate” located approximately 10 m above the ground was reached with acceptable vertical and horizontal speeds of 4 m/s and 5 m/s, respectively. It was also established that optic flow sensing methods can be used successfully to cope with temporary sensor blinding and poor lighting conditions.

## I. INTRODUCTION

Automatic landing on extraterrestrial bodies is still an extremely hazardous and challenging task, even if the lander is equipped with the most advanced navigation and guidance systems. However, landing on the Moon, Mars and celestial bodies is often a vital part of scientific space missions. Entry, descent and landing on extraterrestrial bodies is controlled in various ways. Early missions used radar to control landing (e.g. Apollo 11). Newer approaches include lidar techniques [1], [2] and visual techniques [3], [4], [5], [6], [7], [8], [9] often supported with inertial measurements. In addition, vision-based navigation plays a key role when it is required to detect an extraterrestrial target from afar. Processing video-data fast enough to extract the requisite

self motion data is a technically challenging task, especially in view of the tight aerospace restrictions involved in terms of the processing power, size and payload of the embedded electronics. Alternative solutions to this problem have been suggested by the neuronal and sensory systems of flying insects, which are able to navigate swiftly in unfamiliar environments by relying heavily on the angular speed of the images that sweep backward across their view-field [10], [11], which is known as the optic flow (OF) (Fig. 2) [12]. Bees, for example, use the OF to avoid obstacles [13], [14], to control their speed [15], [16] and height [17], [18], and to cruise and land [19], [18], [20]. These insects’ motion is sensed by Elementary Motion Detectors (EMDs), which process the OF by comparing the signals collected by adjacent visual sensors [21], [22]: the artificial EMD used here was a genuine airborne OF sensor.

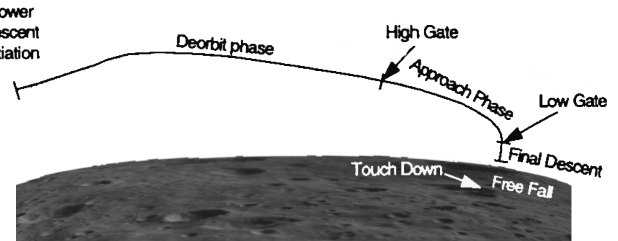


Fig. 1. Reference Descent Trajectory to land on the Moon. The trajectory was divided into 4 phases: the de-orbit phase to reach “high gate”, the approach phase to reach “low gate” located at a height of 10m, the final descent, and the free fall to touchdown. This study focused on the automation of the “high gate” to “low gate” approach phase, based on the use of motion vision cues. Modified from [23].

The use of visual cues to guide spacecrafts’ extraterrestrial soft landing performances has been recently investigated by several authors [24], [25], [3]. These systems either use visually assisted inertial navigation systems [25] or compute the optic flow by means of an optical correlator [3], [9] or extract information from a single camera [25], [26]. By contrast, the autopilot described here extends the previously described EMD-based OCTAVE-autopilot principles [27], [28] to a lunar lander.

In the present study, the optic flow regulator has been completely redesigned to stabilize the Lander: a state-space representation including a state feedback and a nonlinear observer was used to cope with lander characteristics. In addition, the validity of our neuromorphic approach to landing control was tested with lunar images, and the ability of a simplified simulated lander to arrive safely at “low gate” during the

Manuscript submitted September 15, 2009

This work was supported partly by CNRS (Life Science; Information and Engineering Science and Technology), by the Uni. of the Mediterranean, by ESA under Ariadna contract 08-6303b, and by EU via the CURVACE project. The project CURVACE acknowledges the financial support of the Future and Emerging Technologies (FET) programme within the Seventh Framework Programme for Research of the European Commission, under FET-Open grant number: 237940.

F. Valette, F. Ruffier, S. Viollet are with the Biorobotics Dept. at the Institute of Movement Sciences, CNRS / Uni. of the Mediterranean, CP938, 163 ave. Luminy, 13288 Marseille Cedex 09, France florent.valette@gmail.com, {franck.ruffier, stephane.viollet}@univmed.fr

T. Seidl is with the Advanced Concepts Team, European Space Agency (ESA), 2201 AZ Noordwijk, The Nederlands tobias.seidl@gmail.com

lunar approach phase was confirmed (Fig. 1). “Low gate” position was defined as the landing height at which direct visual contact with the landing site is obscured by the dust raised by the thrusters, for instance. Visual navigation is impossible from “low gate” onwards and alternative non-visual techniques are therefore required.

In the present setting, flight was controlled by keeping the OF perceived by the EMD as close as possible to a previously set point value. The EMD output signal was used directly to adjust the engine’s thrust, and hence the horizontal and vertical speeds. The autopilot then enabled the lander to safely decrease its horizontal speed, vertical speed, and height with a rough estimation of the initial height and vertical speed at high gate to initialize the non-linear observer. This estimation may be done by applying classical equations of the celestial mechanics. In the application in question, the autopilot also has to cope with:

- the natural instability of the lander,
- the large variations in altitude and speed due to the large working domain of application,
- the presence of many non-linearities in the lander.

The mechanisms involved in optic-flow processing are described in detail in the section II, and the autopilot control scheme is presented in the section III. Lastly, the results of the simulation experiments are given and discussed in the section IV.

## II. EMD-BASED OPTIC FLOW MEASUREMENT USING PANGU

### A. Pure translational Optic Flow (OF)

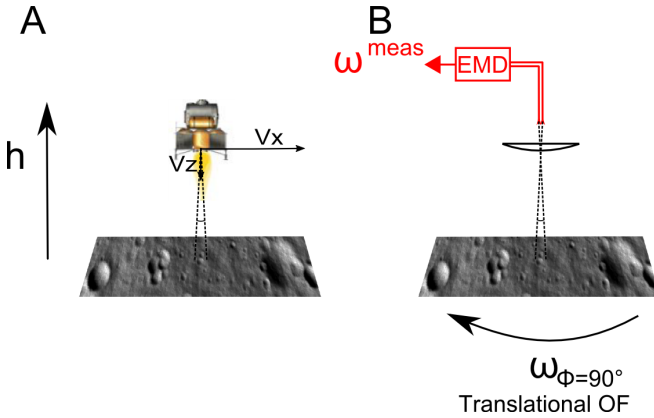


Fig. 2. Optic Flow (OF) generated and measured above the lunar surface. (A) The ventral OF perceived by the lander flying at ground speed  $V_x$  and ground height  $h$  is the angular speed  $\omega_{\Phi=90^\circ}$  at which a point on the lunar surface directly below seems to move in the opposite direction. The lunar ground shown here is a sample image generated by the PANGU software program. (B) A simulated minimalistic OF sensor used on-board the lander. This sensor comprises a micro lens and two fly-inspired photoreceptors acting as elementary motion detectors (EMDs). Its output  $\omega^{meas}$  is used by the spacecraft autopilot as a feedback signal (Fig. 4).

The present simulation focused on a simplified lander flying above a lunar surface generated by the PANGU software program [29]. The lander was equipped with an

elementary eye composed of a single OF sensor pointing downwards at an elevation  $\Phi$  (the angle between X-axis and the optical axis of the sensor). This lander was taken to have a limited number of degrees of freedom (two translations along the X and Z axes and one rotation around the pitch axis). During its simulated flight above the lunar surface, the sighted lander measured its self-motion in terms of the angular velocities  $\omega_{\Phi}$  generated:

$$\omega_{\Phi} = \frac{v}{D} \cdot \sin(\Psi + \Phi) \quad (1)$$

where  $v$  is the speed of the lander,  $\Psi$  is the angle between the lander’s speed vector and its horizontal projection,  $D$  is the distance from the ground in the gaze direction, and  $\Phi$  is the angular elevation of the gaze direction. The lander moved as dictated by a ground speed vector  $\vec{V}_x$  and a vertical speed vector  $\vec{V}_z$  along the lunar surface images generated by PANGU. In the present setup, the gaze was stabilized ( $\Phi = 90^\circ$ ) vertically downwards to cope with any pitch manoeuvres of the lander (Fig 2):

- $D$  becomes the local height  $h$  with respect to the ground (the “ground height”),
- $v \cdot \sin(\Psi + \Phi)$  becomes the ground speed  $V_x$ .

Since any rotation due to the spacecraft is compensated for, the OF sensor will receive purely translational flow information, consisting of the angular velocity of the lunar surface projected onto the ventral OF sensor. Therefore, the translational OF was simply defined by the ratio between the ground speed and the ground height, as expressed in the following equation 2 (see Fig.1b in [28]).

$$\omega_{\Phi=90^\circ} = \frac{V_x}{h} \quad (2)$$

### B. Bio-inspired OF processing using images from the Moon

The simulated visual environment consisted of lunar surface images generated by PANGU, taking the position of the observer and that of the light source into account. The simulated lunar surface was not smooth and could include deep craters (up to 40m deep). The images generated by PANGU contained 256 gray-scale levels and had a resolution of  $256 \times 256$  pixels; one square pixel corresponded to  $0.1^\circ \times 0.1^\circ$  in the field of view.

The OF sensor was mounted pointing downwards with respect to the simulated lander’s symmetry axis. This sensor consisted of two photoreceptors (i.e. two pixels) driving an Elementary Motion Detector (EMD). The visual axes of the two photoreceptors diverged by an inter-receptor angle  $\Delta\phi = 2^\circ$ . The angular sensitivity of each photoreceptor obeyed a 2-D Gaussian function mimicking the angular sensitivity of a fly’s photoreceptor with an acceptance angle (the angular width at half height)  $\Delta\rho = 2^\circ$ , as described by [30]. Each photoreceptor covered a field of view measuring  $5^\circ \times 5^\circ$ .

The photoreceptor output was computed at each simulation time step (1ms) by convolving the lunar surface image given by PANGU with the 2-D Gaussian filter. The simulated EMDs used spatio-temporal filtering steps as well as a contrast thresholding step to assess the OF [21], [22], [31].

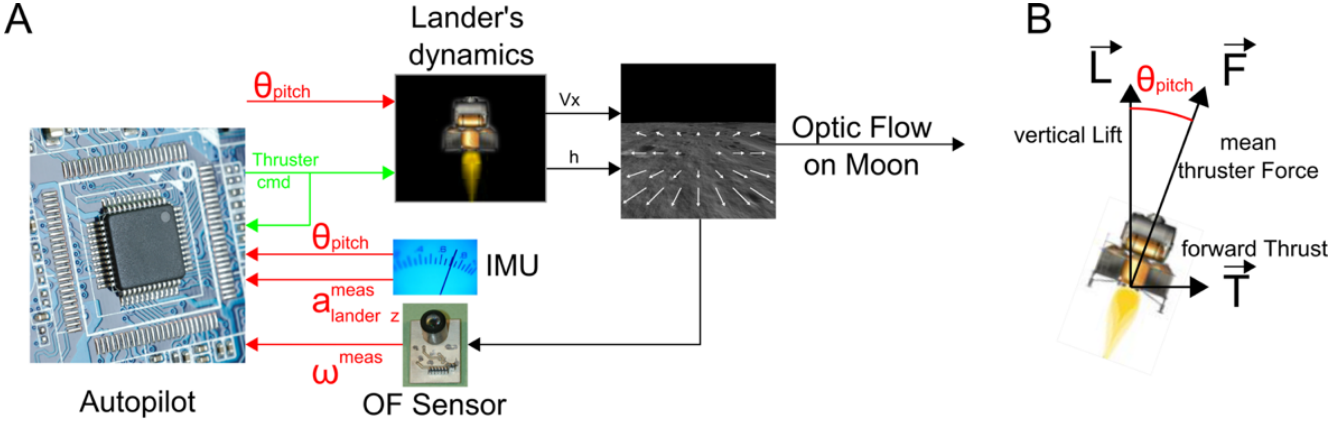


Fig. 4. (A) Sketch of the OF-based lunar landing autopilot. The digital autopilot received the following inputs: the pitch angle  $\theta_{pitch}$  (given by an IMU), the measured OF  $\omega^{meas}$  (given by an EMD) and the vertical acceleration  $a_{lander\ z}^{meas}$  (given by an accelerometer). In addition, the controller imposed the thrust level and the lander's pitch. (B) The lander decreased or increased its forward thrust by pitching backward or forward, respectively. The vertical lift was directly affected by the pitch.

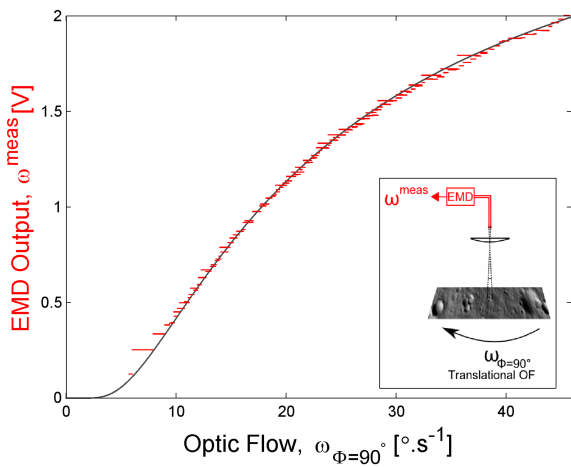


Fig. 3. EMD Input/Output characteristics resulting from the lunar image velocities generated by PANGU. Analog EMD output (in Volts) (red lines) versus the OF (i.e., an angular velocity in  $^{\circ}/s$ ). This figure shows the EMD responses to several motion stimuli at various angular speeds. These data were collected using images produced by PANGU. The simulated circuit based on Franceschini's time-of-travel EMD scheme delivered a monotonically increasing response (red plot) with respect to the angular velocity (see equation 3). In order to obtain these input/output response characteristics on the Moon, we applied ground speeds ranging from 50 to 300m/s to the lander at various altitudes (from 100 to 500m). Deviations from the theoretical functional characteristics (grey curve) obtained from (3) were mainly due to the lunar craters simulated by PANGU (which were up to 40m deep).

The working principles of the Franceschini's time-of-travel EMD scheme used here were based on the results of studies on the fly's eye, in which electrophysiological recordings were performed while light micro stimulation was applied to the retina [32]. The range of the EMD responses was calibrated by tuning the time constant  $\tau_{EMD}$  (see equation 3) of the decreasing exponential in order to be able to measure the exact OF generated by the lander. Depending on the speed and altitude of the lander during the landing

phase, the OF therefore ranged between  $10^{\circ}/s$  and  $30^{\circ}/s$ . Depending on the inter-receptor angle  $\Delta\phi$ , the time constant  $\tau_{EMD}$  of the final low pass filter (figure 3 in [31]) was adjusted to  $\tau_{EMD} = 0.1s$ . With these parameters, the OF sensor's characteristics are shown in figure 3. The OF sensor's response was a monotonically increasing function of the angular velocity with an order of magnitude ranging from  $4.5^{\circ}/s$  to  $45^{\circ}/s$ , as described by the following equation:

$$\omega^{meas} = k \cdot e^{-\frac{\Delta\phi}{\omega_{\Phi} \cdot \tau_{EMD}}} \quad (3)$$

where  $k = 3.08V$ ,  $\Delta\phi = 2^{\circ}$ ,  $\tau_{EMD} = 0.1s$ .

### III. OPTIC FLOW REGULATOR

#### A. Dynamic model for a lunar lander

The autopilot presented here consisted mainly of a similar OF regulator to that previously described [27], [28] operating in the vertical plane ( $x$ ,  $z$ ), which controlled the spacecraft's mean thruster force. To stabilize the lander, it was necessary to cope with non-linearities and the inherent instability. Since there is no atmosphere on the Moon, no friction, wind or drag forces have to be dealt with. In the present model, the heave and surge dynamics were coupled via the lander's pitch (Fig. 4B). The mean Force  $\overline{F}$  resulting from the thrusters can be expressed in terms of the vertical lift  $L$  (see Fig. 4B), as follows:

$$L = F \cdot \cos \theta_{pitch} \quad (4)$$

The thrusters could produce only positive forces and the maximum thrust was limited to  $100 \cdot m_{lander}$  [N]. The transfer function  $G_{thruster}(s)$  describes the thruster dynamics between the mean thruster force and the thruster's control input signal, as follows:

$$G_{thruster}(s) = \frac{F(s)}{Thruster\ cmd(s)} = \frac{1/\tau_{thruster}}{1/\tau_{thruster} + s} \quad (5)$$

where  $\tau_{thruster} = 0.1s$ .

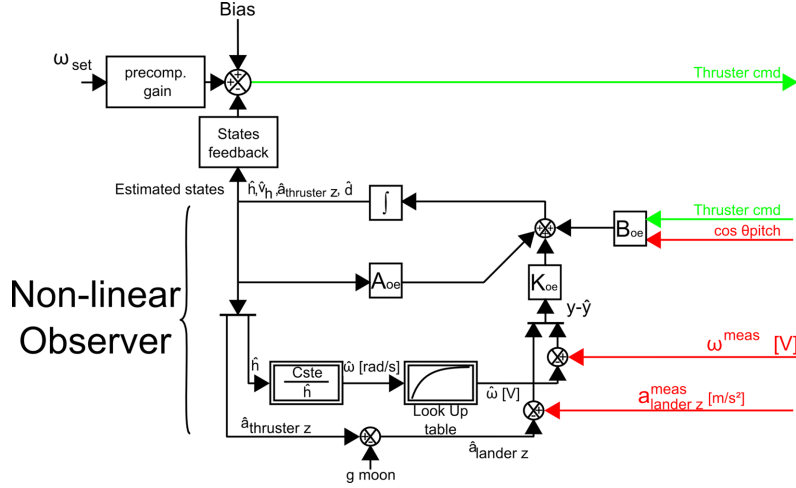


Fig. 5. The present autopilot used a non-linear observer to provide the feedback control scheme with the state estimates. The observer was nonlinear since  $\omega$  is by definition an inverse function of the controlled variable  $h$ . The state estimate of the OF in  $rad/s$  was computed in terms of the ratio between a constant (the ground speed at a given working point) and the estimated height of the lander  $\hat{h}$ . The optic flow was then obtained via a look-up table. The measured acceleration of the lander  $a_{landerz}^{meas}$  served only to improve the state estimation. The estimated acceleration  $\hat{a}_{landerz}$  was obtained by subtracting the approximate gravity on the Moon  $g_{Moon}$  from the estimated acceleration induced by the thruster  $\hat{a}_{thrusterz}$ .

By applying the principles of dynamics to the heave axis, we obtain the following equation:

$$L - m_{Lander} \cdot g_{Moon} = m_{Lander} \cdot a_{landerz} \quad (6)$$

where  $g_{Moon}$  is the lunar gravity constant ( $g_{Moon} = 1.63m/s^2$ ),  $m_{lander} = 10^3kg$  is the lander's mass and  $a_{landerz}$  is the lander's acceleration in the lunar reference frame.

From equations 6 and 5, it is possible to obtain the transfer function describing the heave dynamics, i.e, the transfer between the altitude of the lander and the control signals transmitted to the thruster engine:

$$G_z(s) = \frac{z(s)}{Thruster_{cmd}(s)} = \frac{1}{s^2} \cdot \left[ \left( \frac{1/\tau_{thruster}}{1/\tau_{thruster} + s} \cdot \cos \theta_{pitch} \right) - g_{Moon} \right] \quad (7)$$

In the lander model, the following state vector was used:

$$X = \begin{bmatrix} h \\ V_z \\ a_{thrusterz} \end{bmatrix}$$

and the following input  $u = \begin{bmatrix} L \\ m_{Lander} \end{bmatrix}$ . Based on the equation 6, we can write:

$$\left\{ \begin{array}{l} \dot{a}_{thrusterz} = \frac{1}{\tau_{thruster}} \cdot \left[ \frac{L}{m_{Lander}} - a_{thrusterz} \right] \\ \dot{V}_z = a_{thrusterz} - g_{Moon} \\ \dot{h} = V_z \end{array} \right. \quad (8)$$

where  $V_z$  is the lander's linear speed along the  $z$  axis and  $a_{thrusterz}$  is the thruster's acceleration.

The state space matrix  $A_p$ ,  $B_p$  and a disturbance vector  $g$

can be deduced from the equation 8 as follows:

$$\begin{aligned} \dot{X} &= A_p \cdot X + B_p \cdot u - g \\ \begin{bmatrix} \dot{h} \\ \dot{V}_z \\ \dot{a}_{thrusterz} \end{bmatrix} &= \begin{bmatrix} 0 & 1 & 0 \\ 0 & 0 & 1 \\ 0 & 0 & \frac{-1}{\tau_{thruster}} \end{bmatrix} \cdot \begin{bmatrix} h \\ V_z \\ a_{thrusterz} \end{bmatrix} \\ &\quad + \begin{bmatrix} 0 \\ 0 \\ \frac{1}{\tau_{thruster}} \end{bmatrix} \cdot \begin{bmatrix} L \\ m_{Lander} \end{bmatrix} - \begin{bmatrix} 0 \\ g_{Moon} \\ 0 \end{bmatrix} \end{aligned} \quad (9)$$

The present moonlander was modelled by the thruster dynamics and a pure double integration between the acceleration and the altitude, using the state-space approach. The autopilot, which operated on the basis of a single OF measurement (that of the ventral OF), consisted of a visuomotor feedback loop driving the mean thruster force. The vertical lift and the forward thrust were coupled and the loop therefore controlled both the heave and surge axes. The pitch angle  $\theta_{pitch}$  was controlled by an external system: the lander pitched backwards from  $-60^\circ$  to  $-30^\circ$  while landing. The autopilot (Fig. 5) was composed of (i) a precompensation gain, (ii) a non linear state observer, and (iii) a state feedback gain. The non linear state observer estimated the state vector  $X$  on the basis of the ventral OF,  $\omega^{meas}$ , the lander acceleration,  $a_{landerz}$  and the lander pitch,  $\theta_{Pitch}$ . The complete regulator combined the estimated states with the full state feedback control loop.

### B. Control law based on full state feedback

The autopilot kept the ventral OF of the simulated lander at the set point  $\omega_{set}$ . This set point was compared with the product of the estimated state vector  $\hat{X}$  (Eq.11) and the state feedback gain  $L_{sf}$  to generate the thruster command. The

state feedback gain was calculated using the minimization criterion in the *lqr* method (Linear quadratic regulator), using the following matrix:  $A_{sf} = A_p$ ,  $B_{sf} = B_p$  and  $C_{sf} = \begin{bmatrix} K_{lin} & 0 & 0 \end{bmatrix}$  and the state-cost matrix  $Q_c = \begin{bmatrix} 7.8 \cdot 10^{-4} & 0 & 0 \\ 0 & 0 & 0 \\ 0 & 0 & 0 \end{bmatrix}$  and  $R_c = [1]$ . To compute the  $C_{sf}$  matrix, we linearized the expression for the OF near a set point. Here the set point was  $h_{lin} = 200m$ ,  $V_{x_{lin}} = 50m/s$  and  $\omega = 14.3^\circ/s$ . The OF was defined as an inverse function of  $h$ . We therefore used the slope of the tangent to linearize the expression as follows:

$$K_{lin} = V_{x_{lin}} \cdot \frac{d}{dh} \left( \frac{1}{h} \right)_{h=h_{lin}} = -\frac{V_{x_{lin}}}{h_{lin}^2}. \quad (10)$$

### C. Non linear state observer

Since the system is observable, a state observer for  $\hat{\bar{X}}$  can be formulated as follows:

$$\dot{\hat{\bar{X}}} = A_o \cdot \hat{\bar{X}} + B_o \cdot u + K_o \cdot (y - \hat{y}) \quad (11)$$

$$\hat{y} = C_o \cdot \hat{\bar{X}} + D_o \cdot u \quad (12)$$

where  $A_o = A_{sf}$ ,  $B_o = B_{sf}$ ,  $C_o = \begin{bmatrix} C_{sf} \\ 0 & 0 & 1 \end{bmatrix}$ ,  $D_o = [0]$  and  $K_o$  (Observer gain) was also computed with the *lqr* method, using the  $A_o$  and the  $C_o$  matrix. As shown in figure 5, the estimator requires the value of the lander's acceleration  $a_{lander_z}$ .

To achieve an integral control, the augmented state vector  $\hat{\bar{X}}$  was thus defined:  $\hat{\bar{X}}_e = \begin{bmatrix} \hat{\bar{X}} \\ d \end{bmatrix}$ . The new state matrix could therefore be written as follows:

$$\left\{ \begin{array}{l} A_{oe} = \begin{bmatrix} A_o & B_o \\ 0 & 0 & 0 & 0 \end{bmatrix} \\ B_{oe} = \begin{bmatrix} B_o \\ 0 \end{bmatrix} \\ C_{oe} = \begin{bmatrix} C_o & 0 \end{bmatrix} \end{array} \right. \quad (13)$$

The new state feedback gain  $L_{sfe}$  was equal to:

$$L_{sfe} = [ L_{sf} \ 1 ] \quad (14)$$

The observer gain was computed in the case of the extended state using the same method, with the new state matrix ( $A_{oe}$  and  $C_{oe}$ ).

The acceleration of the lander ( $\hat{a}_{lander_z}$ ) was estimated by subtracting the lunar gravity ( $g_{Moon}$ ) from the estimated engine thrust ( $\hat{a}_{thruster_z}$ ) (Fig 5).

The observer is initialized using a rough estimation of the initial height and vertical speed at high gate. The observer

tolerates an uncertainty of about 20% in the estimation of the height and vertical speed.

### D. Automatic landing example

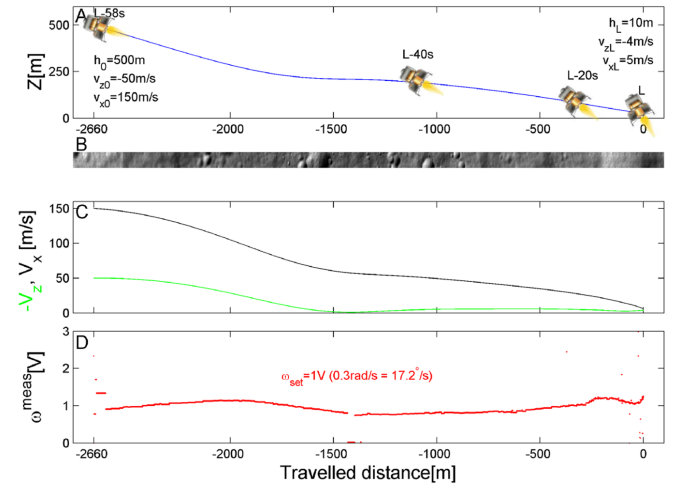


Fig. 6. Automatic landing based on a biomimetic OF sensor combined with a bio-inspired strategy. The automatic landing lasted 58.4s, starting from an initial height of 500m, with an initial ground speed of 150m/s and an initial vertical speed of 50m/s. (A) Vertical trajectory in the longitudinal plane. At  $t_l = 58.4s$  (58.4s before reaching "low gate" at time  $t_l$ ), the pitch angle  $\theta_{pitch}$  was equal to  $-60^\circ$  and decreased exponentially to  $-30^\circ$  at  $t_l = 10s$ . The ensuing decrease in the ground speed (150m/s to less than 10m/s at  $t_l = 10s$ ) automatically decreased the ground height and the vertical speed in order to keep the measured OF near the set-point. (B) lunar surface as presented to the simulated lander during the entire landing phase. (C) Ground speed  $V_x$  (black) and Vertical speed  $V_z$  (green) monitored throughout the landing phase. (D) Output  $\omega_{meas}$  of the OF sensor was also monitored during the landing phase,  $\omega_{set} = 1V (0.3rad/s = 17.2^\circ/s)$ .

To ensure a soft landing, the lander had to reach a distance of approximately 10 meters from the ground (i.e., the "low gate") at a residual velocity of one meter per second in both the horizontal and vertical directions. Thanks to the biomimetic autopilot, the lander reached "low gate" with greatly reduced horizontal and vertical speeds approximately equal to the required values (Fig. 6). The lunar surface perceived by the lander consisted of gray-scale images generated by PANGU. In our simulation, we adopted an initial altitude  $Z_o = 500m$ , an initial ground speed  $V_{x_0} = 150m/s$  and an initial vertical speed  $V_{z_0} = -50m/s$ . The pitch angle  $\theta_{pitch}$  decreased exponentially from  $-60^\circ$  to  $-30^\circ$ , and the forward speed therefore decreased quasi-exponentially (Figure 6C), as did the vertical speed (Figure 6C), since its integral  $h$  was reduced quasi-exponentially to hold the measured OF  $\omega_{meas} = v_z/h$  around the set point value  $\omega_{set}$  (Figure 6D).

The spacecraft's simulated approach took 58.4s, where  $t_l$  is the time required to reach "low gate". The lander reached "low gate" at a final ground speed  $V_{x_{t_l}} = 5m/s$  and a final vertical speed  $V_{z_{t_l}} = -4m/s$ ; the distance travelled by the lander during the landing was 2660 meters. The final horizontal and vertical speeds are slightly higher than expected to strictly satisfy the speeds' criterion at low gate (1m/s) in a near future.

## IV. RESULTS

### A. Influence of initial conditions

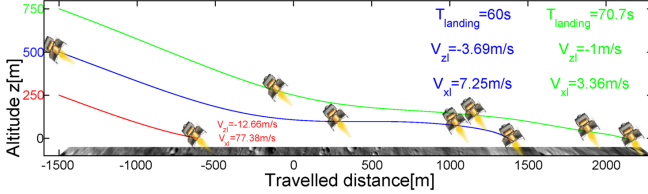


Fig. 7. Automatic landing from various initial altitudes. The simulation was initiated at altitudes of 750m (green), 500m (blue), and 250m (red) under regular lighting conditions (initial ground speed 150m/s, initial vertical speed  $-50\text{m/s}$ ). The lander is plotted here every 20s until it reached low gate. With an initial altitude of 250m, the lander will probably crash, since “low gate” was reached after 8s at a high ground speed of  $77.4\text{m/s}$  and a high vertical speed of  $-12.7\text{m/s}$ . With an initial altitude of 500m, the lander reached “low gate” in 60s with a ground speed of  $7.25\text{m/s}$  and a vertical speed of  $-3.69\text{m/s}$ . With an initial altitude of 750m, the lander safely reached “low gate” in 70.7s with a ground speed of  $3.36\text{m/s}$  and a vertical speed of  $-1\text{m/s}$ .

The influence of the initial altitude (with a given initial ground speed and vertical speed,  $V_{x0} = 150\text{m/s}$  and  $V_{z0} = -50\text{m/s}$ , respectively) is shown in Figure 7. Since pitching reduced the forward speed, the lander automatically adjusted its thrust to maintain the ventral OF at the set point throughout the landing. With initial altitudes of 500m and 750m, the lander successfully reached “low gate” with an acceptable ground speed and vertical speed. In the case of a very low starting altitude (here: 250m), the ventral OF was initially too high for the autopilot. It therefore reached “low gate” with a high ground speed  $V_{x_l} = 77.4\text{m/s}$  and a high vertical speed  $V_{z_l} = -12.7\text{m/s}$ : these values were too high for safe landing to be possible.

### B. Influence of the pitching law

The landing duration depended greatly on the pitching law profile: it significantly influenced the spacecraft’s behaviour in terms of both the speed and the fuel consumption. The landing performances were studied with various pitching laws, which were defined as follows:

- Exponentially decreasing law with various time constants ( $\tau = 15\text{s}$ ,  $\tau = 20\text{s}$  and  $\tau = 25\text{s}$ ) from  $-60^\circ$  to  $-30^\circ$ ,
- Linearly decreasing law from  $-60^\circ$  with various slopes ( $1$ ,  $0.5$ ,  $0.25$ ,  $0.125^\circ/\text{s}$ ),
- Constant pitch of  $-60^\circ$ .

These laws were applied to the setup described above and automatic landing was performed under the following initial conditions:  $h_0 = 500\text{m}$ ,  $V_{z0} = 50\text{m/s}$ ,  $V_{x0} = 150\text{m/s}$ . The upper thruster saturation limit was never reached with any of the pitching laws tested. To assess the quality of the landing performances, the following final parameters of the lander were compared, as shown in Tab. I:

- the landing duration,
- the final vertical speed at “low gate”,

- the final horizontal speed at “low gate”,
- a fuel-consumption criterion, which is the integral of the thrust (Eq. 15),
- the final pitch in each trial,

The fuel consumption criterion was defined as follows:

$$\text{Consumption} = \int_0^{t_l} \text{Thruster}_{cmd}(t) \cdot m_{Lander} dt \quad (15)$$

Table I shows that a slow linear decrease in pitch ( $0.25$  or  $0.125^\circ/\text{s}$ ) resulted in faster landing and an appropriate decrease in the vertical and horizontal speeds that reached a few meters per second at “low gate”. We are considering to introduce an additional breaking phase in order to reach final speeds of  $1\text{m/s}$ .

### C. Low solar elevation

The landing trajectory was compared between two lighting conditions:

- nominal light condition with the sun elevation equals to  $15^\circ$ ,
- low light condition with the sun elevation equals to  $1.5^\circ$  (south pole).

In our PANGU-based simulations, we observed that even under challenging lighting conditions (e.g. with a sun elevation of  $1.5^\circ$ ), EMD-based OF processing results in successful landing (Fig. 8). It was concluded that even lighting conditions such as those encountered during lunar southpole landing might be compatible with neuromorphic technology. The OF values  $\omega^{meas}$  recorded were similar to those obtained under nominal lighting conditions (Figure 8C and F). However, the EMD updating rate depends on the presence of contrast within the sensor’s range of sensitivity. Under very weak lighting conditions, the OF sensor output would not be updated because the contrast would not be detected by the sensor.

### D. Temporary absence of OF measurements

According to our simulations, this system resists temporary blinding of the sensor (Fig. 9). Blinding may occur during the approach as the result of crossing a zone which does not provide any visual contrast, e.g. a valley, a crater or the shaded side of a hill. As long as this blinding is of limited duration (up to  $6\text{s}$  in this setup), the plant will successfully reach “low gate”; when it encounters a sensor blinding level of  $9\text{s}$ , the plant arrives at “low gate” at a speed which is too high to be able to land safely.

## V. CONCLUSIONS

Here we have presented the first simulations in which neuromorphic principles have been applied to monitoring and processing the optic flow in an autonomous visual-based extraterrestrial landing scenario. In the present autopilot, biological principles such as motion extraction and OF regulation were used to land a simulated spacecraft in a lunar

TABLE I  
COMPARISON BETWEEN LANDING PERFORMANCES WITH VARIOUS PITCHING LAWS.

| Pitching Law            | Exponential  |              |              | Linear      |               |                |                 | Constant |
|-------------------------|--------------|--------------|--------------|-------------|---------------|----------------|-----------------|----------|
| Parameter               | $\tau = 25s$ | $\tau = 20s$ | $\tau = 15s$ | $1^\circ/s$ | $0.5^\circ/s$ | $0.25^\circ/s$ | $0.125^\circ/s$ | —        |
| Landing duration [s]    | 55.2         | <b>58.4</b>  | 74.7         | 63.3        | 38.8          | 30.3           | 25.4            | 21.4     |
| Final $V_{x_1}$ [m/s]   | 4.07         | <b>7.25</b>  | 4.8          | 5.91        | 4.01          | 2.12           | 3.98            | 10.87    |
| Final $V_{z_1}$ [m/s]   | -3.72        | <b>-3.69</b> | -6.43        | -5.27       | -4.52         | -3.75          | -2.69           | -4.68    |
| Consumption/mlander     | 201.4        | <b>200</b>   | 222.7        | 210         | 182.2         | 176            | 170.9           | 160.7    |
| Pitch at touch down [°] | -33.3        | <b>-31.6</b> | -30.2        | -30         | -40.8         | -52.4          | -56.4           | -60      |
| Comment                 | Typical      | Typical      | Overshoot    | Slow        | Nice          | Nice           | Very Short      | Too Fast |

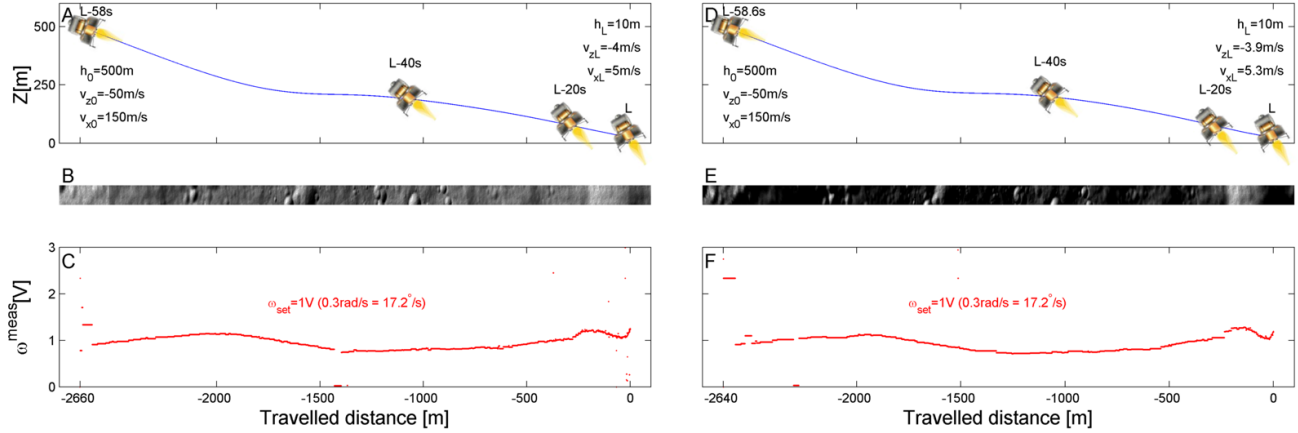


Fig. 8. Comparison between automatic landing under nominal and south-pole lighting conditions. (A) Lander trajectory under nominal lighting conditions and with an initial ground speed  $V_{x0} = 150m/s$ , an initial vertical speed  $V_{z0} = -50m/s$  and an initial altitude  $Z_0 = 500m$  (cf. Fig. 6) (B) PANGU-generated lunar surface under nominal lighting conditions. (C) Output  $\omega^{meas}$  of the OF sensor monitored during the landing under nominal lighting conditions. The OF was relatively constant throughout,  $\omega_{set} = 1V (0.3rad/s = 17.2^\circ/s)$ . (D) Landing trajectory obtained using the same initial settings but under lighting conditions resembling those pertaining at the lunar south pole, i.e. sun elevation at  $1.5^\circ$ . (E) PANGU generated lunar surface with sun elevation at  $1.5^\circ$ . The terrain was the same as that presented in Fig. 8C. (F) The OF measured  $\omega^{meas}$  remained the same as in (C) despite the challenging lighting conditions, which were similar to those pertaining at the south pole of the Moon.  $\omega_{set} = 1V (0.3rad/s = 17.2^\circ/s)$ .

scenario. The results obtained show that appropriate settings enabled a lander equipped with this biomimetic autopilot to safely reach “low gate”, even if the final ground and vertical speeds of these first simulations are slightly higher than expected.

The main differences with previous visual landing methods are the low optical resolution, the lightweight optics consisting of only two pixels and the high temporal resolution of the visual processing system presented here. Thanks to the biomimetic electronic circuits such as EMD used here, all the computations were performed at a sampling frequency of 1kHz. In addition, the present autopilot monitored only the optic flow and thus regulated the spacecraft’s flight without any need to specify the speed and distance, and hence without any need for bulky, power-consuming sensors. The simulated lander navigated on the basis of only a few parameters: the pitch, the vertical acceleration, the ventral optic flow with a rough estimation of the initial height and vertical speed at high gate to initialize the non-linear observer. It was established that the OF regulator held the perceived OF close to a previously chosen set point by acting on the mean thruster force. As a result, the lander’s ground

speed and vertical speed decreased automatically during the landing phase due to the coupling between the heave and surge dynamics, and the lander therefore reached “low gate” at low speed.

The performances of the present controller were found to be robust despite the presence of various disturbances. Safe and soft landing occurred even at a low sun elevation of  $1.5^\circ$ , which is typical that occurring at landing sites near the Moon’s south pole. Temporary sensor blinding can be compensated for to a certain extent at this early stage of development. Variations in the initial flight conditions occurring during the trajectory can also be compensated for successfully (up to a point) by the system presented here. During all the simulation experiments, it is worth noting that PANGU generated a highly realistic Moon terrain, including valleys and craters with depths of up to -40m.

As these first simulations nicely demonstrated the high potential of our bio-inspired approach, the next steps will focus on reducing again the approach speeds to “low gate” below  $1m/s$ , and we will probably introduce an additional braking phase. Next to piloting the spacecraft, guidance and navigation issues need to be addressed. Therefore we suggest

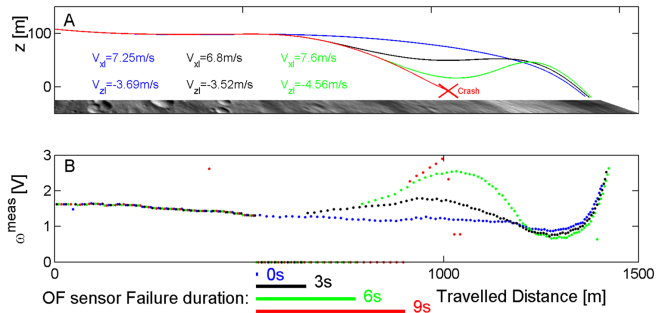


Fig. 9. Effects of transient sensory blinding. The controller was confronted with sensor failures of various durations: Blue line: no failure, black: 3s, green: 6s, and red: 9s without OF readings, respectively. (A) Lander trajectory and the lunar surface generated by PANGU. In the failure-free control situation, the lander reached “low gate” in 60s with a vertical speed of  $-3.69\text{m/s}$  and a ground speed of  $7.25\text{m/s}$ . When the OF sensor was blinded for 3s i.e., the reading values were zero (black line), the lander reached “low gate” in 60.4s at a vertical speed of  $-3.52\text{m/s}$  and a ground speed of  $6.8\text{m/s}$ . When the sensor blinding lasted 6s (green line), the lander reached “low gate” in 60.3s with a vertical speed of  $-4.56\text{m/s}$  and a ground speed of  $7.6\text{m/s}$ . However, when the sensor reading at zero was extended to 9s (red line), the lander crashed after 37.6s at a vertical speed of  $-10.9\text{m/s}$  and a ground speed of  $36.2\text{m/s}$ . (B) OF  $\omega^{\text{meas}}$  monitored during the landing. When the sensor became functional again, the controller managed to re-establish the OF at the set point after 3s and 6s of blinding, but failed after a period of 9s without a reliable OF signal.

to enlarge the sensory field of view and address hazard detection and avoidance mechanisms based on EMD-technology. Further vibration tests should determine the robustness of a gimbal mounted OF sensor made of Franceschini’s time-of-travel EMD scheme. In addition, we suggest simulations with three degrees of freedom including a second feedback loop to control the lander’s pitch through optic flow. Finally we suggest to implement high level target localization features for pinpoint landing capability.

#### ACKNOWLEDGEMENTS

We thank N. Franceschini for his fruitful comments and J. Blanc for revising the English manuscript.

#### REFERENCES

- [1] S. Parkes and V. Silva, *GNC sensors for planetary landers : a review*, special pu ed. European Space Agency, 2001, pp. 744–752.
- [2] S. Parkes, M. Dunstan, D. Matthews, I. Martin, and V. Silva, “Lidar-based gnc for planetary landing: Simulation with pangu,” in *DASIA (Data Systems in Aerospace)*, 2003.
- [3] K. Janschek, V. Tchernykh, and M. Beck, “Performance analysis for visual planetary landing navigation using optical flow and dem matching,” in *AIAA Guidance, Navigation and Control Conference Exhibit*, 2006.
- [4] S. Melloni, M. Mammarella, J. Gil-Fernández, P. ColmenarejoMatellano, and M. Homeister, “Gnc solutions for next-moon lunar lander mission,” in *21st ISSFD*, no. 1, Toulouse, 2009, pp. 1–15.
- [5] D. Meng, C. Yun-feng, W. Qing-xian, and Z. Zhen, “Image Processing in Optical Guidance for Autonomous Landing of Lunar Probe,” in *ICIUS 2007*, Bali, Indonesia, 2007, pp. ICIUS2007-A001.
- [6] A. I. Mourikis, N. Trawny, S. I. Roumeliotis, A. E. Johnson, A. Ansar, and L. Matthies, “Vision-aided inertial navigation for spacecraft entry, descent, and landing,” *IEEE Transactions on Robotics*, vol. 25, no. 2, pp. 264–280, April 2009.
- [7] Y. Shang and P. Palmer, “The dynamic motion estimation of a lunar lander using optical navigation,” no. 1, pp. 1–14.
- [8] S. Strandmoe, T. Jean-Marius, and S. Trinh, “Toward a vision based autonomous planetary lander,” pp. AIAA-99-4154.
- [9] V. Tchernykh, M. Beck, and K. Janschek, “An embedded optical flow processor for visual navigation using optical correlator technology,” in *Proceedings of the 2006 IEEE/RSJ, international conference on intelligent robot and systems*, 2006.
- [10] G. A. Horridge, “The evolution of visual processing of seeing system,” *Proc. Roy. Soc. Lond. B*, vol. 230, pp. 279–292, 1987.
- [11] N. Franceschini, “Towards automatic visual guidance of aerospace vehicles : from insects to robots,” *Acta Futura*, no. 3, pp. 15–34, 2009.
- [12] J. Gibson, *The perception of the visual world*. Boston: Houghton Mifflin, 1950.
- [13] J. Serres, M. G. F. Ruffier, and N. Franceschini, “A bee in the corridor: centering and wall-following,” *Naturwissenschaften*, vol. 95, pp. 1181–1187, 2008.
- [14] M. V. Srinivasan, M. Lehrer, W. H. Kirchner, and S. Zhang, “Range perception through apparent image speed in freely flying honeybees,” *Vis. Neurosci.*, vol. 6, pp. 519–535, 1991.
- [15] R. Preiss, “Motion parallax and figural properties of depth control flight speed in an insect,” *Biol. Cyb.*, vol. 57, pp. 1–9, 1987.
- [16] E. Baird, M. V. Srinivasan, S. Zhang, and A. Cowling, “Visual control of flight speed in honeybees,” *J. Exp. Biol.*, vol. 208, pp. 3895–3905, 2005.
- [17] E. Baird, M. V. Srinivasan, S. Zhang, R. Lamont, and A. Cowling, “Visual control of flight speed and height in honeybee,” *LNAI*, vol. 4095, pp. 40–51, 2006.
- [18] N. Franceschini, F. Ruffier, and J. Serres, “A bio-inspired flying robot sheds light on insect piloting abilities,” *Current Biology*, vol. 17(4), pp. 329–335, 2007.
- [19] M. Srinivasan, S. Zhang, M. Lehrer, and T. Collett, “Honeybee navigation en route to the goal: visual flight control and odometry,” *J. Exp. Biol.*, vol. 199, pp. 237–244, 1996.
- [20] M. Srinivasan, S. Zhang, J. Chahl, E. Barth, and S. Venkatesh, “How honeybees make grazing landings on flat surfaces,” *Biological Cybernetics*, vol. 83(3), pp. 171–183, 2000.
- [21] C. Blanes, *Appareil visuel élémentaire pour la navigation à vue d'un robot mobile autonome*. Marseille: Master thesis in Neurosciences (DEA in French), Neurosciences, Univ. Aix-Marseille II, Advisor: N. Franceschini, 1986.
- [22] ———, “Guidage visuel d’un robot mobile autonome d’inspiration biologique 2nde partie,” Ph.D. dissertation, Thèse de doctorat, Grenoble: Institut National Polytechnique de Grenoble (INP Grenoble), Advisor: N. Franceschini, 1991.
- [23] T. Jean-Marius and S. E. Strandmoe, “Integrated vision and navigation for a planetary lander,” *AEROSPATIAL*, Espace et Dfense, Les Mureaux-France. ESA, Estec, Noordwijk-The Netherlands, Tech. Rep., 1998.
- [24] S. Thakoor, J. Chahl, M. V. Srinivasan, L. Young, F. Werblin, B. Hine, and S. Zornetzer, “Bioinspired engineering of exploration systems for nasa and dod,” *Artificial Life*, vol. 8, no. 4, pp. 357–369, 2002.
- [25] A. Mourikis, N. Trawny, S. Roumeliotis, A. Johnson, and A. A. L. Matthies, “Vision-aided inertial navigation for spacecraft entry, descent and landing,” *IEEE transaction on robotics*, vol. 25, pp. 264–280, 2009.
- [26] D. Meng, C. Yun-feng, W. Qing-xian, and Z. Zhen, “Image processing in optical guidance for autonomous landing of lunar probe,” pp. 1–10, 2009.
- [27] F. Ruffier, S. Viollet, S. Amic, and N. Franceschini, “Bio-inspired optical flow circuits for the visual guidance of micro-air vehicles,” in *Proc. of IEEE Int. Symposium on Circuits and Systems (ISCAS)*, Bangkok, Thailand, 2003, pp. Vol. III, pp. 846–849.
- [28] F. Ruffier and N. Franceschini, “Optic flow regulation: the key to aircraft automatic guidance,” *Robotics and Autonomous Systems*, vol. 50(4), pp. 177–194, 2005.
- [29] S. M. Parkes, I. Martin, M. Dunstan, and D. Matthews, “Planet surface simulation with pangu,” in *8th International Conference on Space Operations (SpaceOps 2004)*, Montreal, Canada, May 17-21, 2004.
- [30] A. W. Snyder, “Acuity of compound eyes: Physical limitations and design,” *J. comp. physiol. A*, vol. 116, pp. 161–182, 1977.
- [31] N. Franceschini, F. Ruffier, J. Serres, and S. Viollet, *Aerial vehicles*. In-Tech, 2009, ch. Optic flow based visual guidance: from flying insects to miniature aerial vehicles, pp. 747–770.
- [32] N. Franceschini, A. Richle, and A. L. Nestour, *Directionally Selective Motion Detection by Insect Neurons*. D.G. Stavenga, R.C. Hardie, Eds., Springer, Berlin, 1989, pp. 360–390.